Optics Letters

Laser ablation of silicon induced by a femtosecond optical vortex beam

Jijil J. J. Nivas,[1,2] He Shutong,[1,3] K. K. Anoop,[1,2] A. Rubano,[1,2] R. Fittipaldi,[4] A. Vecchione,[4] D. Paparo,[2] L. Marrucci,[1,2] R. Bruzzese,[1,2] and S. Amoruso[1,2,*]

[1]Dipartimento di Fisica, Università di Napoli Federico II, Complesso Universitario di Monte S. Angelo, Via Cintia, I-80126 Napoli, Italy
[2]CNR-SPIN UOS Napoli, Complesso Universitario di Monte S. Angelo, Via Cintia, I-80126 Napoli, Italy
[3]Ultrafast Laser Laboratory, Key Laboratory of Opto-Electronic Information Technical Science of Ministry of Education, College of Precision Instruments and Opto-Electronics Engineering, Tianjin University, Tianjin 300072, China
[4]CNR-SPIN, UOS Salerno, Via Giovanni Paolo II 132, I-84084 Fisciano, Italy
*Corresponding author: amoruso@na.infn.it

Received 29 June 2015; revised 7 September 2015; accepted 11 September 2015; posted 11 September 2015 (Doc. ID 243819); published 7 October 2015

We investigate laser ablation of crystalline silicon induced by a femtosecond optical vortex beam, addressing how beam properties can be obtained by analyzing the ablation crater. The morphology of the surface structures formed in the annular crater surface allows direct visualization of the beam polarization, while analysis of the crater size provides beam spot parameters. We also determine the diverse threshold fluences for the formation of various complex microstructures generated within the annular laser spot on the silicon sample. Our analysis indicates an incubation behavior of the threshold fluence as a function of the number of laser pulses, independent of the optical vortex polarization, in weak focusing conditions.

OCIS codes: (140.3295) Laser beam characterization; (320.2250) Femtosecond phenomena; (320.7130) Ultrafast processes in condensed matter, including semiconductors.

http://dx.doi.org/10.1364/OL.40.004611

Laser ablation with intense femtosecond (fs) pulses is a valuable tool in many applications, for example, direct surface structuring of solid targets [1,2], generation of nanoparticles [3,4], and fabrication of nanostructured films by deposition of the ablation plume [5,6]. In particular, direct fs laser surface processing attracts increasing interest as an effective way to fabricate surface structures at nano- and micro-scales on metals and semiconductors. Typically, a fs laser beam with a Gaussian intensity profile is focused onto the surface of the solid target under study. The focal length of the focusing lens is usually quite long, generating a spot diameter of 10 μm or larger [1,2]. Ablation occurs when the peak laser fluence is larger than the ablation threshold of the material. The properties of the ablation process are related to the beam characteristics and for laser beams with a Gaussian intensity profile are obtained by a well-established method based on the analysis of the lateral dimensions of the crater produced on the target [7,8]. In fact, crater analyses allow for determining beam waist, peak fluence of the laser pulse, as well as the fluence threshold for ablation of the target material and the conditions for the formation of specific surface structures. All these parameters are fundamental for an accurate description of the experimental conditions and for a clear analysis of the investigated processes.

Recently, laser beams with non-Gaussian intensity profiles are gaining attention as a novel prospect in laser–matter interactions and related applications [9–11]. In particular, the current development of efficient beam converters generating powerful fs optical vortex pulses offers the possibility of observing new experimental aspects in this emerging topic [11–15]. The use of optical vortex (OV) beams in fs laser ablation and surface structuring has recently led to the generation of subwavelength ring structures on silicon or glass [12,13] and the production of surface microstructures on stainless steel, silicon, and copper [15–18]. These microstructures display a clear relationship with the spatial distribution of laser beam intensity and polarization.

Laser-induced structures and crater profiles have been used as a direct way to diagnose intense, cylindrical vector beams in the focal plane [13–15,19–21]. Actually, there is no research addressing the optimal conditions for the formation of the diverse surface structures produced during laser irradiation of a solid target with a fs OV beam. Therefore, a detailed understanding of the diverse threshold fluences for ablation and for the formation of the various surface microstructures is essential to achieve an accurate and reliable determination of the OV beam properties.

Here, we report an analysis of crater and surface structures produced in direct fs laser ablation of silicon with an OV beam, demonstrating an effective method for characterizing the OV beam properties. Silicon is selected as a case study, being the most basic and studied semiconductor material widely applied in mechanical, optical, and electronic devices. The optical

vortex beam is generated via spin-to-orbital conversion of the angular momentum of light by using a q-plate [22,23].

Figure 1(a) reports a schematic of the experimental setup. The laser source is a Ti:Sa laser system delivering linearly polarized ≈35 fs pulses at 800 nm. An OV beam, carrying an orbital angular momentum (OAM) $\ell = \pm 1$, is produced by a q-plate with a topological charge $q = 1/2$. The inset in Fig. 1(a) reports an image of the beam spatial intensity distribution as acquired by a beam profiler. It is characterized by an annular spatial profile, with a central region of zero intensity due to an undefined phase on the OV beam axis. Figure 1(b) shows the normalized intensity variation of the fluence along a diameter. Direct fs laser ablation of silicon (100) was induced by focusing the OV beam on the target surface with a lens of 75 mm focal length, in air. The target was mounted on a XY-translation stage located perpendicular to the laser beam direction [Fig. 1(a)]. An electromechanical shutter provided the selection of the desired number of laser pulses, N, applied to the same spot on the target. The morphology of the irradiated surface was analyzed by a scanning electron microscope.

Figure 2 reports an example of a typical SEM micrograph of the silicon surface irradiated area for $N = 100$, for an azimuthal polarization. It shows the formation of a shallow, annular crater reflecting the beam shape. A complex surface morphology is observed in Fig. 2, with various annular regions characterized by different surface textures. The central region with a radius $R_{in} \approx 12$ μm is decorated by a large number of nanoparticles and corresponds to the central part of the beam with an intensity well below the target ablation threshold. The external circle of the ablated area has a radius $R_{ex} \approx 58$ μm and marks the transition to a fluence lower than the ablation threshold. The region just beyond R_{ex} is also densely decorated by nanoparticles. The ablated crater defined by the annulus going from R_{in} to R_{ex}, presents an inner region with a width of ≈25 μm characterized by microwrinkles aligned along the beam polarization, surrounded by two adjacent areas where subwavelength ripples are aligned perpendicular to the laser polarization. The inset of Fig. 2 shows a zoomed view of these ripples. The radial widths of these two areas are ≈7 μm (inner) and ≈12 μm (outer), respectively. The diverse widths of these two regions is likely due to the different fluence spatial gradients in the central ($r < r_p$) and outer ($r > r_p$) regions of the OV beam profile [see Fig. 1(b)].

The polarization of the OV beam can be appropriately changed by varying the angle between the linear polarization

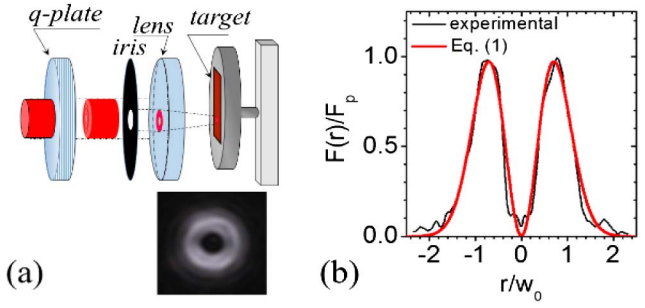

Fig. 1. (a) Schematic of the experimental setup. The inset shows the vortex beam spatial intensity profile. (b) Normalized spatial profile of the pulse fluence along the diameter of the beam (in units of the beam waist w_0).

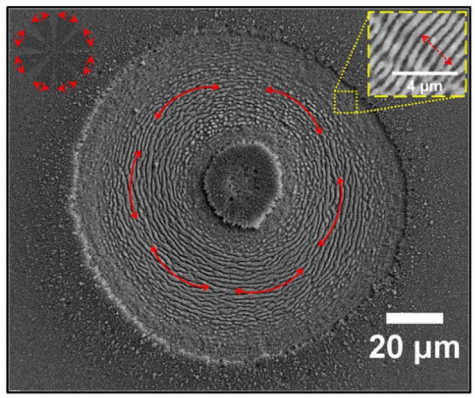

Fig. 2. SEM micrograph of the target surface after irradiation with an azimuthally polarized OV beam at an energy $E_0 \approx 30$ μJ, after $N = 100$ laser pulses. The red arrows in the upper left corner sketch the state of polarization, while those on the pattern indicate the local laser beam polarization. The inset in the upper right corner shows the morphology of the ripples formed in the outer region of the beam spot.

of the input Gaussian beam and the q-plate axis, which eventually affects the surface structure morphology. As an example, Fig. 3 reports two SEM micrographs of the silicon surface after irradiation with radially and spirally polarized OV beams, at $N = 100$ and $E_0 = 50$ μJ. In all cases, microwrinkles aligned along the local beam polarization are present in the higher fluence region, while ripples perpendicular to the polarization are formed in the low fluence areas. This, in turn, suggests a deterministic relationship between orientation and characteristic size of the surface structure and local polarization and fluence of the OV beam. It is worth noting that earlier studies mainly focused on subwavelength ripples [1,2,8,9,14–16,21], while more detailed analyses of microwrinkles produced by fs Gaussian beams started only very recently [24,25]. Our findings indicate that the two structures are ubiquitous to fs laser ablation of silicon. Hence, we investigated the threshold fluence for the formation of both structures and how it depends on the OV beam properties.

The spatial profile of the pulse fluence F(r), along the diameter of an OV beam with $\ell = \pm 1$, as a function of the radial coordinate r is described by the following distribution [11]:

$$F(r) = 2^2 E_0 \frac{r^2}{\pi w_0^4} e^{-\frac{2r^2}{w_0^2}}, \quad (1)$$

where E_0 is the beam energy and w_0 the waist of the corresponding fundamental Gaussian beam. Equation (1) approximates the experimental profile rather well, as shown in Fig. 1(b). The spatial distribution in Fig. 1(b) shows the

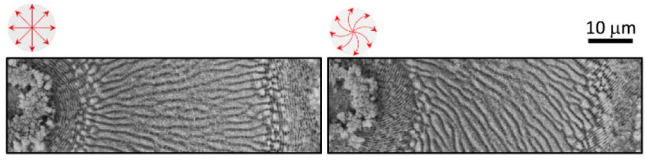

Fig. 3. Zoomed views of a portion of the ablation crater for radial (left panel) and spiral (right panel) polarization of the OV beam at $E_0 = 50$ μJ and $N = 100$. The red arrows sketch the state of polarization.

presence of a null fluence at the beam center and of two symmetric peaks at the positions $\pm r_p$, where r_p is given by

$$r_p = \frac{w_0}{\sqrt{2}}. \quad (2)$$

The corresponding peak fluence value F_p is

$$F_p = F(r_p) = 2e^{-1}\frac{E_0}{\pi w_0^2} \approx 0.736\frac{E_0}{\pi w_0^2}. \quad (3)$$

We discuss first the variation of the internal, R_{in}, and external, R_{ex}, radii as a function of the OV laser pulse energy E_0. R_{in} and R_{ex} marks the threshold for ablation and ripples formation. Figure 4 reports two examples of the experimental dependence of R_{in} and R_{ex} as a function of E_0, for $N = 20$ and $N = 100$, in the case of irradiation with an azimuthally polarized OV beam. One can observe a progressive reduction of the width of the ablated annulus ($R_{ex} - R_{in}$) as the energy E_0 decreases. This annulus eventually degenerates into a limiting circumference with a radius $R_{in} = R_{ex} = r_p$ when E_0 reaches the threshold level E_{th}, and the peak fluence F_p corresponds to the threshold fluence F_{th}, i.e.,

$$F_{th} = 2e^{-1}\frac{E_{th}}{\pi w_0^2}. \quad (4)$$

The variation of R_{in} and R_{ex} versus E_0 can be modeled by solving the equation $F(r) = F_{th}$. An analytical solution for this equation does not exist. However, fits to the experimental data can be obtained through a numerical resolution and are reported as solid curves in Fig. 4(a). The experimental data are well described by the two branches departing from the point of coordinates (E_{th}, r_p) and corresponding to R_{in} and R_{ex} versus E_0. The beam waist w_0 and the threshold fluence F_{th} were used as fitting parameters, thus obtaining $w_0 = (46 \pm 2)$ μm, and the values of F_{th} reported in Fig. 4(b) for three different N values. We observe a progressive reduction of F_{th} with N. This trend is explained as an incubation behavior described by the dependence $F_{th,N} = F_{th,1} \times N^{\xi-1}$, where ξ is a material-dependent incubation factor ($\xi = 0.84$ was reported for silicon [8]). The solid line in Fig. 4(b) is a fit to the incubation dependence, yielding $F_{th,1} = (0.27 \pm 0.04)$ J/cm^2 and $\xi = (0.81 \pm 0.05)$, consistent with the previous results of Bonse *et al.* for silicon [8].

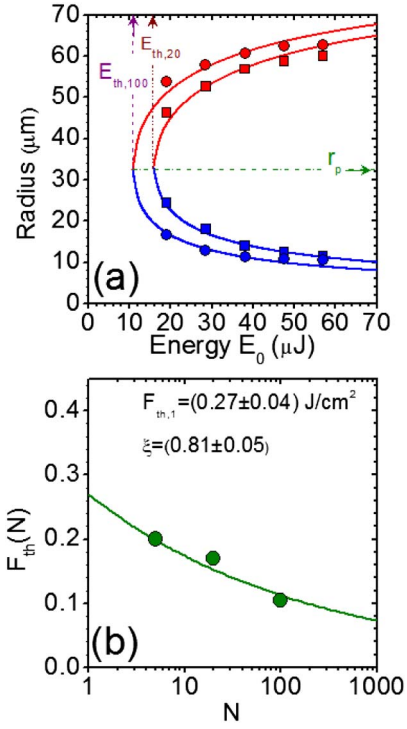

Fig. 4. (a) Examples of the variation of the internal (R_{in}, blue data points) and external (R_{ex}, red data points) radii as a function of the OV beam energy E_0 for two different numbers of pulses N: squares, $N = 20$; circles, $N = 100$. (b) Variation of the fluence threshold F_{th} with the number of pulses N. The uncertainties on the experimental data points are contained within their respective size. The line is a fit to the dependence $F_{th,N} = F_{th,1} \times N^{\xi-1}$ with the values of the fitting parameters shown in the figure.

Figure 5 reports a zoomed view of a radial portion of the SEM image of Fig. 2 and the corresponding spatial profile of the laser pulse fluence. It illustrates the close relationship between the surface texture and the local value of the laser fluence. The central area of the annular crater with $F(r) > \Phi_{th,100}(\approx 0.24$ J/cm$^2)$ is covered by the wrinkles, while the ripples are present in the two low fluence regions with $F_{th,100} < F(r) < \Phi_{th,100}$, where $\Phi_{th,100}$ is the threshold fluence for wrinkle formation at $N = 100$. This suggests that (i) appropriate shaping of the fluence profile can be used to fabricate complex surface patterns; (ii) an accurate determination of the laser beam parameters (e.g., spot size and peak fluence) can be obtained and correlated with the local laser pulse fluence by means of the structured surface texture; and (iii) in weak focusing conditions, the two-dimensional vector field structure of intense fs laser beams in a plane orthogonal to the propagation axis can be visualized directly.

Finally, we also analyzed the variation of the internal and external radii with the number of pulses N, for OV beams characterized by azimuthal, radial, and circular polarizations, at a pulse energy $E_0 \approx 50$ μJ. The different polarization patterns were generated by appropriate rotation of the linear polarization of the input beam before the q-plate or by using a quarter-waveplate. The results are summarized in Fig. 6. One can observe a progressive rise in the width of the ablated annulus ($R_{ex} - R_{in}$) as the number of laser pulses N increases, independent of the specific polarization. The solid curves in Fig. 6 show a model dependence obtained by taking into account the

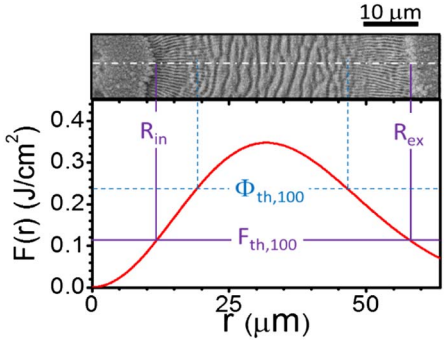

Fig. 5. Zoomed view of a portion of Fig. 2 and the corresponding spatial distribution of the laser pulse fluence illustrating the dependence of the surface texture on the local value fluence. $F_{th,100}$ marks the fluence threshold and the corresponding internal R_{in} and external R_{ex} radii, while $\Phi_{th,100}$ indicates a central region characterized by wrinkles.

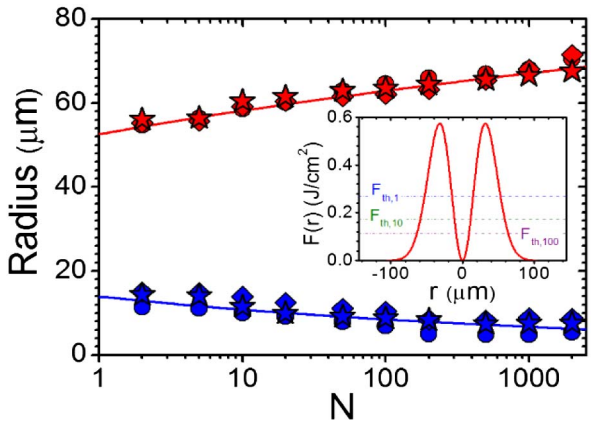

Fig. 6. Variation of the internal (R_{in}, blue data points) and external (R_{ex}, red data points) radii as a function of the number of pulses N for the OV beam with azimuthal (circles), radial (diamond), and circular (stars) polarizations, at a pulse energy $E_0 \approx 50$ μJ. The solid lines are model dependence according to the incubation effect. Inset: OV beam spatial profile and fluence threshold values $F_{th,N}$ for $N = 1$, 10, and 100 as predicted by the incubation dependence $F_{th,N} = F_{th,1} \times N^{\xi-1}$, with $F_{th,1} = 0.27$ J/cm^2 and $\xi = 0.81$.

progressive reduction of the fluence threshold due to the incubation effect and illustrated in the inset for $N = 1$, 10, and 100. The model prediction describes the experimental results rather well.

Our experimental findings suggest a weak dependence on the threshold fluences for ablation/ripples formation and ripples-to-wrinkles transition on the OV beam polarization, in our experimental conditions. Nonetheless, an earlier report addressed a significant dependence of the ablation efficiency of silicon on the handedness of light for circularly polarized fs OV beams, in tight focusing geometry [13]. This last effect is associated with the generation of a longitudinal electric field component, whose intensity significantly depends on light handedness. In weak focusing conditions, the fraction of beam energy associated with the longitudinal component of the electric field in the focus is negligible. Thus, the OV beam behaves as a 2D vector beam and such an effect disappears in our case.

In conclusion, we carried out an experimental investigation addressing how fs OV beam properties can be determined through the analysis of laser ablation spots. Our experimental findings demonstrate an accurate characterization of intense fs OV beams in weak focusing conditions, as those generally exploited for direct fs laser structuring. Preliminary experiments with OV beams with larger angular momentum confirms the validity of using the imprinted structures as a direct visualization of the polarization pattern in the focal plane. Moreover, the information gathered on the creation of the different surface structures lends itself as a powerful tool for designing specific and well-controlled periodic structures on solid targets. Direct fs laser structuring with Gaussian beams is already successfully exploited in the fabrication of functional surfaces, whose characteristics (e.g., optical, wetting, hydrophobic, and sensing properties, contaminants or pathogens adhesion, and antimicrobial efficacy) are associated with the peculiar laser-produced nano/microstructures (see, e.g., Refs. [1] and [26] and papers therein quoted). The use of fs OV beams might offer further striking possibilities in tailoring and controlling the properties of the surface processed by direct fs laser structuring.

Funding. European Union (Pro-gramme FP7-PEOPLE-2012-CIG, PCIG12-GA-2012-326499-FOXIDUET).

REFERENCES

1. A. Y. Vorobyev and C. Guo, Laser Photonics Rev. **7**, 385 (2013).
2. T.-H. Her, in *Comprehensive Nanoscience and Technology*, D. Andrews, G. Scholes, and G. Wiederrecht, eds. (Elsevier, 2011), Chap. 4.10.
3. S. Amoruso, G. Ausanio, R. Bruzzese, L. Lanotte, P. Scardi, M. Vitiello, and X. Wang, J. Phys. **18**, L49 (2006).
4. N. N. Nedialkov, P. A. Atanasov, S. Amoruso, R. Bruzzese, and X. Wang, Appl. Surf. Sci. **253**, 7761 (2007).
5. M. Sanz, M. López-Arias, J. F. Marco, R. de Nalda, S. Amoruso, G. Ausanio, S. Lettieri, R. Bruzzese, X. Wang, and M. Castillejo, J. Phys. Chem. C **115**, 3203 (2011).
6. S. Amoruso, S. Tuzi, D. K. Pallotti, C. Aruta, R. Bruzzese, F. Chiarella, R. Fittipaldi, S. Lettieri, P. Maddalena, A. Sambri, A. Vecchione, and X. Wang, Appl. Surf. Sci. **270**, 307 (2013).
7. M. Liu, Opt. Lett. **7**, 196 (1982).
8. J. Bonse, S. Baudach, J. Krüger, W. Kautek, and M. Lenzner, Appl. Phys. A **74**, 19 (2002).
9. M. Duocastella and C. B. Arnold, Laser Photonics Rev. **6**, 607 (2012).
10. E. G. Gamaly and A. V. Rode, Prog. Quantum Electron. **37**, 215 (2013).
11. Q. Zhan, Adv. Opt. Photon. **1**, 1 (2009).
12. C. Hnatovsky, V. G. Shvedov, W. Krolikowski, and A. V. Rode, Opt. Lett. **35**, 3417 (2010).
13. C. Hnatovsky, V. G. Shvedov, N. Shostka, A. V. Rode, and W. Krolikowski, Opt. Lett. **37**, 226 (2012).
14. O. J. Allegre, Y. Jin, W. Perrie, J. Ouyang, E. Fearon, S. P. Edwardson, and G. Dearden, Opt. Express **21**, 21198 (2013).
15. Y. Jin, O. J. Allegre, W. Perrie, K. Abrams, J. Ouyang, E. Fearon, S. P. Edwardson, and G. Dearden, Opt. Express **21**, 25333 (2013).
16. K. Lou, S.-X. Qian, X.-L. Wang, Y. Li, B. Gu, C. Tu, and H.-T. Wang, Opt. Express **20**, 120 (2012).
17. K. K. Anoop, A. Rubano, R. Fittipaldi, X. Wang, D. Paparo, A. Vecchione, L. Marrucci, R. Bruzzese, and S. Amoruso, Appl. Phys. Lett. **104**, 241604 (2014).
18. K. K. Anoop, R. Fittipaldi, A. Rubano, X. Wang, D. Paparo, A. Vecchione, L. Marrucci, R. Bruzzese, and S. Amoruso, J. Appl. Phys. **116**, 113102 (2014).
19. C. Hnatovsky, V. Shvedov, W. Krolikowski, and A. Rode, Phys. Rev. Lett. **106**, 123901 (2011).
20. K. Toyoda, F. Takahashi, S. Takizawa, Y. Tokizane, K. Miyamoto, R. Morita, and T. Omatsu, Phys. Rev. Lett. **110**, 143603 (2013).
21. J. Ouyang, W. Perrie, O. J. Allegre, T. Heil, Y. Jin, E. Fearon, D. Eckford, S. P. Edwardson, and G. Dearden, Opt. Express **23**, 12562 (2015).
22. L. Marrucci, E. Karimi, S. Slussarenko, B. Piccirillo, E. Santamato, E. Nagali, and F. Sciarrino, J. Opt. **13**, 064001 (2011).
23. L. Marrucci, C. Manzo, and D. Paparo, Phys. Rev. Lett. **96**, 163905 (2006).
24. S. He, J. JJ. Nivas, K. K. Anoop, A. Vecchione, M. Hu, R. Bruzzese, and S. Amoruso, Appl. Surf. Sci. **353**, 1214 (2015).
25. G. D. Tsibidis, C. Fotakis, and E. Stratakis, Phys. Rev. B **92**, 041405(R) (2015).
26. A. Y. Vorobyev and C. Guo, J. Appl. Phys. **117**, 033103 (2015).